

# Electronic conductivity, oxygen permeability and thermal expansion of $\text{Sr}_{0.7}\text{Ce}_{0.3}\text{Mn}_{1-x}\text{Al}_x\text{O}_{3-\delta}$

I.P. Marozau<sup>a</sup>, V.V. Kharton<sup>a,b,\*</sup>, A.P. Viskup<sup>b</sup>, J.R. Frade<sup>a</sup>, V.V. Samakhval<sup>b</sup>

<sup>a</sup> Department of Ceramics and Glass Engineering, CICECO, University of Aveiro, Campus de Santiago, 3810-193 Aveiro, Portugal

<sup>b</sup> Institute of Physicochemical Problems, Belarus State University, 14 Leningradskaya Str., 220050 Minsk, Belarus

Received 9 January 2005; received in revised form 22 February 2005; accepted 5 March 2005

Available online 16 April 2005

## Abstract

The maximum solubility of aluminum cations in the perovskite lattice of  $\text{Sr}_{0.7}\text{Ce}_{0.3}\text{Mn}_{1-x}\text{Al}_x\text{O}_{3-\delta}$  is approximately 15%. The incorporation of  $\text{Al}^{3+}$  increases oxygen ionic transport due to increasing oxygen nonstoichiometry, and decreases the tetragonal unit cell volume and thermal expansion at temperatures above 600 °C. The total conductivity of  $\text{Sr}_{0.7}\text{Ce}_{0.3}\text{Mn}_{1-x}\text{Al}_x\text{O}_{3-\delta}$  ( $x=0-0.2$ ), predominantly electronic, decreases with aluminum additions and has an activation energy of 10.2–10.9 kJ/mol at 350–850 °C. Analysis of the electronic conduction and Seebeck coefficient of  $\text{Sr}_{0.7}\text{Ce}_{0.3}\text{Mn}_{0.9}\text{Al}_{0.1}\text{O}_{3-\delta}$ , measured in the oxygen partial pressure range from  $10^{-18}$  to 0.5 atm at 700–950 °C, revealed trends characteristic of broad-band semiconductors, such as temperature-independent mobility. The temperature dependence of the charge carrier concentration is weak, but exhibits a tendency to thermal excitation, whilst oxygen losses from the lattice have an opposite effect. The role of the latter factor becomes significant at temperatures above 800 °C and on reducing  $p(\text{O}_2)$  below  $10^{-4}$  to  $10^{-2}$  atm. The oxygen permeability of dense  $\text{Sr}_{0.7}\text{Ce}_{0.3}\text{Mn}_{1-x}\text{Al}_x\text{O}_{3-\delta}$  ( $x=0-0.2$ ) membranes, limited by both bulk ionic conduction and surface exchange, is substantially higher than that of (La, Sr) $\text{MnO}_3$ -based materials used for solid oxide fuel cell cathodes. The average thermal expansion coefficients of  $\text{Sr}_{0.7}\text{Ce}_{0.3}\text{Mn}_{1-x}\text{Al}_x\text{O}_{3-\delta}$  ceramics in air are  $(10.8-11.8) \times 10^{-6} \text{ K}^{-1}$ .

© 2005 Elsevier Ltd. All rights reserved.

**Keywords:** Perovskites; Electrical properties; Ionic conductivity; Fuel cells; Mixed conductor; (Sr, Ce)(Mn, Al) $\text{O}_3$

## 1. Introduction

Electrical power generation in solid oxide fuel cells (SOFCs) provides substantial advantages with respect to traditional energy conversion systems including high efficiency, reliability, modularity, fuel adaptability, low noise and low environmental impact.<sup>1-4</sup> One of the most important challenges in SOFC developments relates to decreasing operation temperatures, which improves long-term performance due to suppressing interaction between different ceramic layers, enhances microstructural stability of electrodes, increases thermodynamic efficiency and enables to use cheaper materials for stack components and SOFC interconnects.<sup>2,3,5,6</sup> As the activation energy of the electrode polarization is

higher than that of the ionic transport, the performance of intermediate-temperature (IT) SOFCs is typically limited by the electrode overpotentials.<sup>7,8</sup> Conventional cathodes based on perovskite-type  $\text{La}_{1-x}\text{Sr}_x\text{MnO}_{3-\delta}$  have a poor oxygen ionic conductivity and insufficient electrocatalytical activity at intermediate temperatures.<sup>9,10</sup>

Recently, a new group of manganites,  $\text{Sr}_{1-x}\text{Ce}_x\text{MnO}_{3-\delta}$ , was suggested as promising cathode materials for SOFCs.<sup>11,12</sup>  $\text{SrMnO}_{3-\delta}$  has a perovskite-type lattice at temperatures above 1400 °C, but undergoes phase transition to hexagonal 4L structure on cooling below 1035 °C.<sup>13</sup> Partial substitution of strontium with Ce cations stabilizes the perovskite phase down to room temperature and increases the total conductivity by two to three orders of magnitude at 600–1000 °C.<sup>11,12</sup> The use of  $\text{Sr}_{1-x}\text{Ce}_x\text{MnO}_{3-\delta}$  may be advantageous due to higher level of the oxygen ionic conductivity with respect to  $\text{La}_{1-x}\text{Sr}_x\text{MnO}_{3-\delta}$ .<sup>14</sup> Although

\* Corresponding author. Tel.: +351 234 370263; fax: +351 234 425300.  
E-mail address: [kharton@cv.ua.pt](mailto:kharton@cv.ua.pt) (V.V. Kharton).

this level is still lower than for other promising SOFC cathodes, such as  $\text{La}_{1-x}\text{Sr}_x\text{Fe}_{1-y}\text{Co}_y\text{O}_{3-\delta}$ ,<sup>14,15</sup> the ionic transport of (Sr, Ce)MnO<sub>3</sub>-based materials can be enhanced by partial substitution of manganese. In particular, as oxygen diffusion in perovskite-type phases occurs via the vacancy mechanism,<sup>16,17</sup> an enhancement in the ionic conduction may be achieved incorporating acceptor-type cations (e.g. Al<sup>3+</sup>), thus increasing oxygen vacancy concentration. Doping with aluminum may also suppress the interaction between Sr<sub>1-x</sub>Ce<sub>x</sub>MnO<sub>3-δ</sub> and stabilized zirconia electrolytes.<sup>11,18</sup> Moreover, heating of the cathode materials is often accompanied with oxygen losses from the lattice, resulting in so-called chemical contribution to the thermal expansion.<sup>19</sup> This may cause interface instability. The substitution of manganese with cations having a constant oxidation state is expected to suppress oxygen stoichiometry variations, as for other transition metal-containing perovskites.<sup>19</sup>

The present work was focused on the study of Sr<sub>1-x</sub>Ce<sub>x</sub>Mn<sub>1-x</sub>Al<sub>x</sub>O<sub>3-δ</sub> system, with particular attention to the properties important for high-temperature electrochemical applications, namely thermal expansion, oxygen transport and electronic conduction.

## 2. Experimental

The powders of Sr<sub>0.7</sub>Ce<sub>0.3</sub>Mn<sub>1-x</sub>Al<sub>x</sub>O<sub>3-δ</sub> ( $x=0-0.3$ ) were prepared via the standard solid-state synthesis route from high-purity Sr(NO<sub>3</sub>)<sub>2</sub>, Ce(NO<sub>3</sub>)<sub>3</sub>·6H<sub>2</sub>O, Mn<sub>2</sub>O<sub>3</sub> and Al(OH)<sub>3</sub>. The stoichiometric amounts of reagents were initially dissolved in dilute nitric acid, followed by drying of the solution and thermal decomposition of the nitrate mixture at 400 °C. The solid-state reactions were conducted at 900–1350 °C in air with multiple intermediate grinding steps. After ball milling, disk-shaped ceramic samples were pressed at 150–200 MPa and then sintered at temperatures from 1320 °C ( $x=0$ ) up to 1450–1500 °C ( $x=0.1-0.3$ ). The density of sintered ceramics was higher than 93% of their theoretical density calculated from X-ray diffraction (XRD) data; the samples for electrical and oxygen permeation measurements were additionally tested for gas-tightness. General characterization of the ceramic materials included scanning electron microscopy coupled with energy dispersive spectroscopy (SEM/EDS), dilatometry, determination of Seebeck coefficient and total conductivity (four-probe dc) as function of the oxygen partial pressure, and steady-state oxygen permeability measurements. Description of the experimental techniques and equipment used for characterization can be found elsewhere (Refs. 19–23 and references cited therein). The Seebeck coefficient and total conductivity were studied in the  $p(\text{O}_2)$  range 10<sup>-19</sup> to 0.5 atm, as described in Refs. 22, 23. The steady-state oxygen permeability was measured at 900–975 °C; the feed-side oxygen partial pressure ( $p_2$ ) for all oxygen permeation measurements was 0.21 atm.

## 3. Results and discussion

### 3.1. Phase composition, microstructure and thermal expansion

XRD studies of Sr<sub>0.7</sub>Ce<sub>0.3</sub>Mn<sub>1-x</sub>Al<sub>x</sub>O<sub>3-δ</sub> ceramics showed the formation of single-phase perovskite for  $x=0-0.1$  (Fig. 1). Further doping leads to segregation of impurity phases, including CeO<sub>2</sub> and SrMn<sub>3</sub>O<sub>6</sub>; the intensity of impurity peaks increases with increasing aluminum content. This indicates that the maximum solubility of Al<sup>3+</sup> cation in the B-sublattice of Sr<sub>0.7</sub>Ce<sub>0.3</sub>MnO<sub>3-δ</sub> is close to 15%. The crystal structure of Sr<sub>0.7</sub>Ce<sub>0.3</sub>Mn<sub>1-x</sub>Al<sub>x</sub>O<sub>3-δ</sub> was identified as tetragonally-distorted perovskite, in agreement with undoped Sr<sub>0.7</sub>Ce<sub>0.3</sub>MnO<sub>3-δ</sub>.<sup>11,12</sup> Therefore, although substitution of manganese with aluminum increases the oxygen vacancy concentration as evidenced by the oxygen permeation data presented further, no destabilization of the perovskite lattice occurs. The unit cell parameters decrease with increasing  $x$  (Table 1) as the ionic radius of Al<sup>3+</sup> is smaller than that of manganese cations.<sup>24</sup> Fig. 1 also shows that structural collapse occurs under strongly reducing conditions: cause reduction of Mn<sup>n+</sup> to lower valence yields significant ionic size changes; the approximate phase stability limit is discussed further.

SEM/EDS inspection of Sr<sub>0.7</sub>Ce<sub>0.3</sub>Mn<sub>1-x</sub>Al<sub>x</sub> ( $x=0-0.1$ ) ceramics showed no presence of phase impurity and/or essential compositional inhomogeneities at the boundaries. The grain size varies in the range 1–2 μm. Representative examples of SEM micrographs of fractured Sr<sub>0.7</sub>Ce<sub>0.3</sub>Mn<sub>0.9</sub>Al<sub>0.1</sub>O<sub>3-δ</sub> are given in Fig. 2.

The dilatometric studies of Sr<sub>0.7</sub>Ce<sub>0.3</sub>Mn<sub>1-x</sub>Al<sub>x</sub> ( $x=0-0.2$ ) materials demonstrated that their thermal expansion in air is almost linear (Fig. 3). For  $x=0$ , a slight increase in the thermal expansion coefficient ( $\alpha$ ) is observed at temperatures above 610–630 °C. This behaviour may be associated with the transition of  $A_{2-x}B_x$  composition from tetragonally distorted to cubic perovskite.

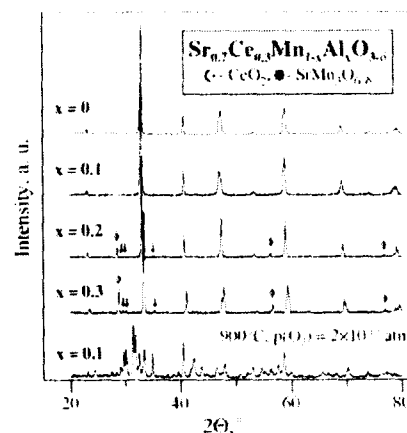


Fig. 1. XRD patterns of Sr<sub>0.7</sub>Ce<sub>0.3</sub>Mn<sub>1-x</sub>Al<sub>x</sub>O<sub>3-δ</sub> in air and after at 1173 K in a H<sub>2</sub>-H<sub>2</sub>O-N<sub>2</sub> flow.

Table 1  
Properties of  $\text{Sr}_{0.7}\text{Ce}_{0.3}\text{Mn}_{1-x}\text{Al}_x\text{O}_{3-\delta}$  ceramics

Composition	Unit cell parameters		Activation energy for total conductivity		Thermal expansion coefficients	
	<i>a</i> (nm)	<i>c</i> (nm)	<i>T</i> (°C)	<i>E<sub>a</sub></i> (kJ/mol)	<i>T</i> (°C)	$\alpha$ ( $\times 10^6$ )
$\text{Sr}_{0.7}\text{Ce}_{0.3}\text{MnO}_{3-\delta}$	0.3838(4)	0.3860(7)	350–850	10.4 ± 0.2	190–830	11.8 ± 0.3
$\text{Sr}_{0.7}\text{Ce}_{0.3}\text{Mn}_{0.9}\text{Al}_{0.1}\text{O}_{3-\delta}$	0.3830(8)	0.3854(9)	360–850 190–360	10.2 ± 0.2 11.9 ± 0.5	100–820	10.8 ± 0.2
$\text{Sr}_{0.7}\text{Ce}_{0.3}\text{Mn}_{0.8}\text{Al}_{0.2}\text{O}_{3-\delta}$	0.3820(6)	0.3832(8)	340–850 180–340	10.9 ± 0.2 12.3 ± 0.7	100–820	10.8 ± 0.1

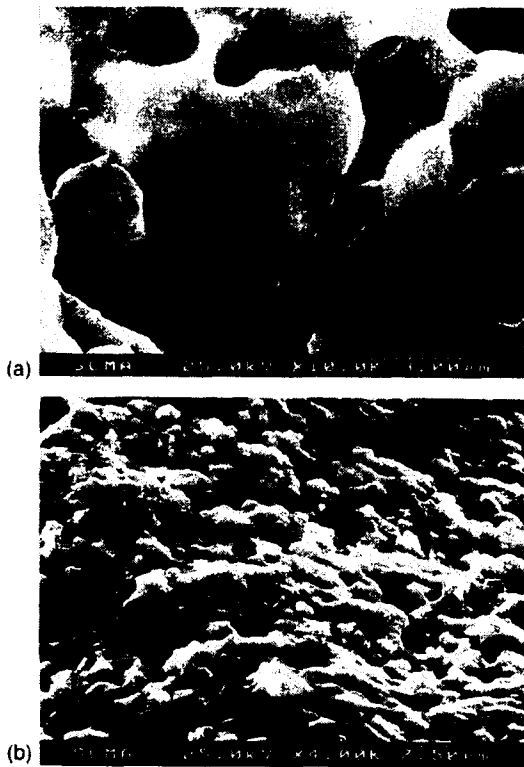


Fig. 2. SEM micrographs of fractured  $\text{Sr}_{0.7}\text{Ce}_{0.3}\text{Mn}_{0.9}\text{Al}_{0.1}\text{O}_{3-\delta}$  ceramics.

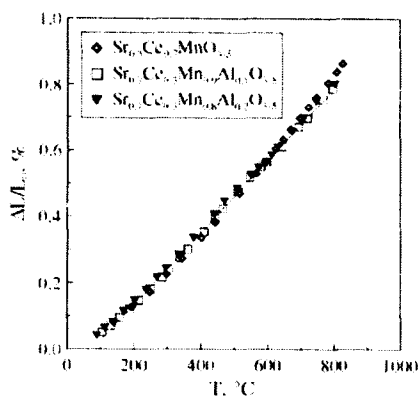


Fig. 3. Dilatometric curves of  $\text{Sr}_{0.7}\text{Ce}_{0.3}\text{Mn}_{1-x}\text{Al}_x\text{O}_{3-\delta}$  ceramics in air.

polymorph, which occurs near 600 °C<sup>11</sup>; another possible reason relates to minor oxygen losses on heating.<sup>19,25</sup> The average TEC values are listed in Table 1. The substitution of manganese decreases TEC values down to  $10.8 \times 10^{-6} \text{ K}^{-1}$ , which provides a good compatibility with commonly used solid electrolytes based on zirconia and ceria.<sup>26,27</sup> Note that the TEC values of alternative mixed-conducting cathodes, including (La, Sr)(Fe, Co)O<sub>3-δ</sub>, are significantly higher than that of  $\text{Sr}_{0.7}\text{Ce}_{0.3}\text{Mn}_{1-x}\text{Al}_x\text{O}_{3-\delta}$  and close to incompatibility with stabilized zirconia solid electrolytes.

### 3.2. Oxygen permeation

Selected results of the oxygen permeation measurements are summarized in Figs. 4 and 5. As expected, the steady-state permeation fluxes (*j*) through  $\text{Sr}_{0.7}\text{Ce}_{0.3}\text{Mn}_{0.9}\text{Al}_{0.1}\text{O}_{3-\delta}$  membranes decrease with increasing membrane thickness (*d*) (Fig. 4A). However, such a decrease is considerably lower than predicted by the integral form of Wagner equation.<sup>28</sup> This is accompanied with increasing specific oxygen perme-

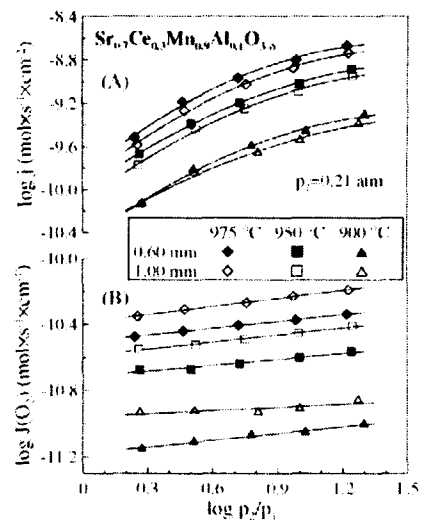


Fig. 4. Dependencies of the oxygen permeation fluxes (A) and specific oxygen permeability (B) of  $\text{Sr}_{0.7}\text{Ce}_{0.3}\text{Mn}_{0.9}\text{Al}_{0.1}\text{O}_{3-\delta}$  ceramics on the oxygen partial pressure gradient.

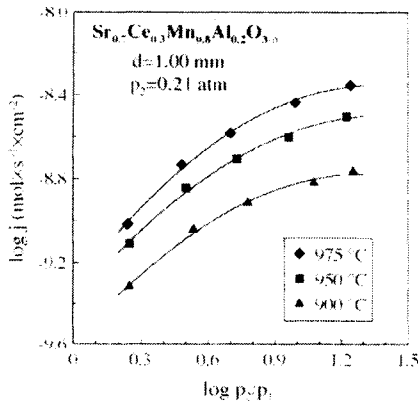


Fig. 5. Dependencies of the oxygen permeation fluxes through  $\text{Sr}_{0.7}\text{Ce}_{0.3}\text{Mn}_{0.8}\text{Al}_{0.2}\text{O}_{3-d}$  ceramics on the oxygen partial pressure gradient.

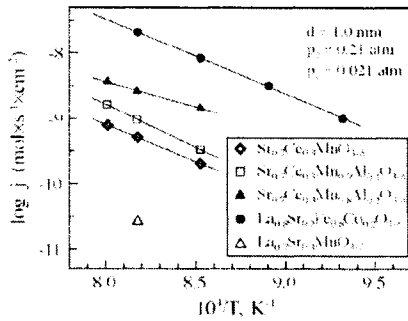


Fig. 6. Temperature dependencies of the oxygen permeation fluxes through  $\text{Sr}_{0.7}\text{Ce}_{0.3}\text{Mn}_{1-x}\text{Al}_x\text{O}_{3-d}$ ,  $\text{La}_{0.7}\text{Sr}_{0.3}\text{MnO}_{3-d}$ <sup>9</sup> and  $\text{La}_{0.8}\text{Sr}_{0.2}\text{Fe}_{0.8}\text{Co}_{0.2}\text{O}_{3-d}$ <sup>14</sup> ceramics under fixed oxygen pressure gradient.

ability  $J(\text{O}_2)$  (Fig. 4B) calculated as

$$J(\text{O}_2) = jd \left[ \ln \left( \frac{p_2}{p_1} \right) \right]^{-1} \quad (1)$$

where  $p_1$  and  $p_2$  are the oxygen partial pressures at the membrane permeate and feed sides, respectively. Such a behaviour unambiguously indicates that the overall oxygen transport is limited both by the bulk ambipolar conductivity and oxygen surface exchange kinetics; the role of the latter factor decreases when the membrane thickness increases.<sup>20,21,28</sup> A significant surface effect is also characteristic for undoped  $\text{Sr}_{0.7}\text{Ce}_{0.3}\text{MnO}_{3-d}$  membranes.<sup>14</sup>

Fig. 6 presents the temperature dependencies of the permeation fluxes through  $\text{Sr}_{0.7}\text{Ce}_{0.3}\text{Mn}_{1-x}\text{Al}_x\text{O}_{3-d}$  under fixed oxygen chemical potential gradient. Increasing aluminum concentration increases oxygen transport, whereas the apparent activation energies are essentially independent of Al content. This suggests an increase in the oxygen nonstoichiometry, caused by the incorporation of acceptor-type  $\text{Al}^{3+}$ . As a result, the ionic ( $\sigma_0$ ) and ambipolar ( $\sigma_{\text{amb}}$ ) conductivities increase on doping, whilst the energetic barrier for ion migration seems essentially unchanged. On the other hand, an enhancement in the surface exchange kinetics might also

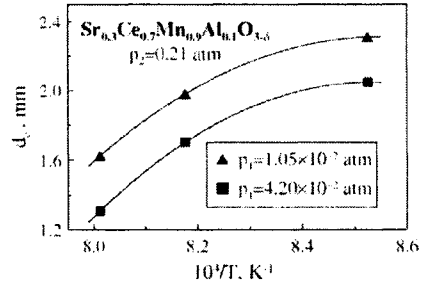


Fig. 7. Temperature dependencies of the critical thickness of  $\text{Sr}_{0.7}\text{Ce}_{0.3}\text{Mn}_{0.9}\text{Al}_{0.1}\text{O}_{3-d}$  membranes (see text).

be expected due to well-known correlations between the exchange currents and bulk oxygen diffusion.<sup>28</sup>

The relative roles of the bulk ambipolar transport and surface exchange may be estimated decomposing the overall driving force, expressed as  $\ln(p_2/p_1)$ , into three contributions associated with membrane bulk and surfaces. The contributions to overcome limitations of surface exchange kinetics can be written as  $\ln(p_2/p'_2)$  for the feed side, with an oxygen partial pressure drop from  $p_2$  to  $p'_2$ , and  $\ln(p'_1/p_1)$  for the permeate side, with a drop from  $p'_1$  to  $p_1$ . The driving force to overcome the resistance to bulk ion transfer is, respectively,  $\ln(p'_2/p'_1)$ . One may express the flux as  $j = k_{\text{cx}}^f \ln(p_2/p'_2) = k_{\text{cx}}^p \ln(p'_1/p_1)$ , where  $k_{\text{cx}}$  is the exchange coefficient, and the superscripts “f” and “p” denote the feed and permeate sides, correspondingly. Under steady-state conditions, the permeation flux through the membrane bulk,  $j = (RT/16F^2d)\sigma_{\text{amb}} \ln(p'_2/p'_1)$ , is equal to the fluxes through the membrane/gas boundaries. This yields

$$\frac{\ln(p_2/p_1)}{j} = \left[ \frac{16F^2}{RT\sigma_{\text{amb}}} \right] d + [k_{\text{cx}}^f]^{-1} + [k_{\text{cx}}^p]^{-1} = \left[ \frac{16F^2}{RT\sigma_{\text{amb}}} \right] (d + d_c) \quad (2)$$

where the critical thickness  $d_c$  corresponds to the transition from exchange control, for thin samples, to bulk transport control, for thicker samples. Eq. (2) was used to extract the estimates of critical thickness  $d_c$  (Fig. 7) and ionic conductivity (Fig. 8) from the data shown in Fig. 4. The values of  $d_c$  are close to 1 mm, thus confirming that the effects of both permeation-determining factors are significant. The critical thickness increases on reducing permeate-side oxygen pressure due to a decrease in the surface exchange coefficient; this trend is typical for most perovskite-type mixed conductors under oxidizing conditions.<sup>28</sup> The estimates of ambipolar conductivity were found  $10^4$ – $10^5$  times lower than the total conductivity (Fig. 9), which shows that  $\sigma_{\text{amb}} \approx \sigma_0$ . Fig. 8 compares the levels of ionic conductivity in  $\text{Sr}_{0.7}\text{Ce}_{0.3}\text{Mn}_{0.9}\text{Al}_{0.1}\text{O}_{3-d}$  and other selected mixed conductors. Note that, contrary to the surface exchange coefficients, the bulk ionic conduction increases on reducing oxygen pressure, corroborating that the  $\sigma_0$  values are determined by the oxygen vacancy concentration (inset in Fig. 8).

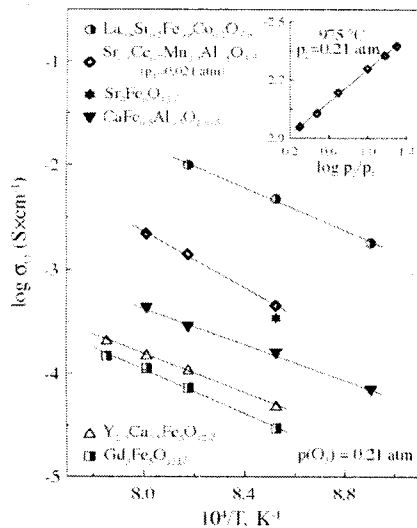


Fig. 8. Temperature dependence of the oxygen ionic conductivity of  $\text{Sr}_{0.7}\text{Ce}_{0.3}\text{Mn}_{1-x}\text{Al}_x\text{O}_{3-\delta}$  ceramics under fixed oxygen pressure gradient, as calculated from the oxygen permeation data (see text). Data on other mixed-conducting materials,<sup>14,41</sup> shown for comparison, all correspond to atmospheric oxygen pressure. The inset shows isothermal variations of the ionic conductivity of  $\text{Sr}_{0.7}\text{Ce}_{0.3}\text{Mn}_{0.9}\text{Al}_{0.1}\text{O}_{3-\delta}$  as function of the oxygen partial pressure gradient.

3.3. Total conductivity in air

The total conductivity ( $\sigma$ ) in the system  $\text{Sr}_{0.7}\text{Ce}_{0.3}\text{Mn}_{1-x}\text{Al}_x\text{O}_{3-\delta}$  decreases with increasing dopant content (Fig. 9). The difference between total and ionic conductivity values (Figs. 8 and 9) unambiguously shows that the electronic contribution is predominant; the ion transference number values are lower than  $10^{-4}$ . The substitution of Mn cations with  $\text{Al}^{3+}$  having a constant oxidation state, leads to partial blocking of electronic transport, which occurs via the  $\text{Mn}^{4+}\text{—O—Mn}^{3+}$  bonds.<sup>29,30</sup> As a re-

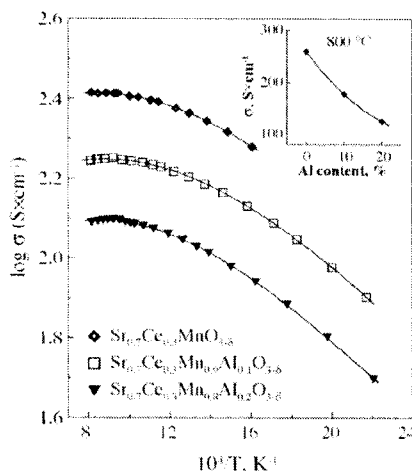


Fig. 9. Temperature dependencies of the total conductivity of  $\text{Sr}_{0.7}\text{Ce}_{0.3}\text{Mn}_{1-x}\text{Al}_x\text{O}_{3-\delta}$  in air. The inset illustrates relationship between the conductivity and composition at 1073 K.

sult, the total conductivity decreases almost linearly with aluminum additions (inset in Fig. 9). The incorporation of 20%  $\text{Al}^{3+}$  into the manganese sublattice lowers the conductivity by a factor of about 0.5. Nevertheless, the level of  $\sigma$  values for  $\text{Sr}_{0.7}\text{Ce}_{0.3}\text{Mn}_{1-x}\text{Al}_x\text{O}_{3-\delta}$  is still in the order of  $120\text{--}250\text{ S cm}^{-1}$  at  $700\text{--}950\text{ }^\circ\text{C}$ , which is sufficient to provide low Ohmic losses at the cathode.<sup>31</sup>

In the low-temperature range, the values of activation energy ( $E_a$ ) for the total conductivity are relatively low and nearly independent of Al content, within the limits of experimental uncertainty (Table 1). The activation energy decreases with increasing temperature, and an apparent transition from semiconducting to pseudo-metallic behaviour is observed at temperatures above approximately  $800\text{ }^\circ\text{C}$ . The negligible dependence of the activation energy on aluminum concentration suggests that  $\text{Al}^{3+}$  cations do not alter significantly the electronic transport mechanism.

3.4. Total conductivity and Seebeck coefficient versus  $p(\text{O}_2)$

The negative sign of the Seebeck coefficient of  $(\text{Sr}, \text{Ce})\text{MnO}_{3-\delta}$  has been interpreted as an indication that electronic transport is n-type.<sup>12</sup> However, the pseudo-metallic conductivity behaviour at high temperatures (Fig. 9) suggests a decrease in charge carrier concentration, as found mostly for perovskite compounds with p-type behaviour.<sup>8,17,21,23,29,30</sup> Moreover, when a single mechanism of the electronic transport is prevailing, the Seebeck coefficient ( $\alpha$ ) can be described by a generic approximate solution using the ratio ( $C_R$ ) between charge carrier concentration and the density of states<sup>32,33</sup>

$$\alpha \approx \pm \frac{k}{e} \ln \left( \frac{1}{C_R} - 1 \right) \tag{3}$$

with positive sign for p-type ( $C_R = p/N$ ) and negative for n-type ( $C_R = n/N$ ) behaviour, where  $N$  is the density of states. Obviously, one cannot distinguish the cases when  $C_R = n/N < 0.5$  or  $C_R = p/N > 0.5$ . For manganites with predominant p-type conduction, one usually ascribes the concentration of electron holes to  $\text{Mn}^{4+}$  content,<sup>29,30</sup> whereas Hashimoto and Iwahara<sup>12</sup> considered trivalent manganese cations as n-type charge carriers in  $(\text{Sr}, \text{Ce})\text{MnO}_{3-\delta}$ , neglecting the contributions of  $\text{Ce}^{3+/4+}$  and  $\text{Mn}^{2+}$  formed due to disproportionation. In these two cases, the corresponding  $C_R$  values are  $p/N \approx [\text{Mn}^{4+}]/[\text{Mn}]$  or  $n/N \approx 1 - [\text{Mn}^{4+}]/[\text{Mn}]$ , where  $[\text{Mn}]$  is the total manganese concentration. Both hypotheses yield

$$[\text{Mn}^{4+}] = \frac{[\text{Mn}]}{1 + \exp(\alpha e/k)} \tag{4}$$

Eq. (4) shows that considering the thermopower sign is insufficient to distinguish n-type or p-type behaviour; an analysis of the charge carrier concentration as a function of temperature and oxygen pressure is necessary for these goals. In particular, whilst the n-type electronic conductiv-

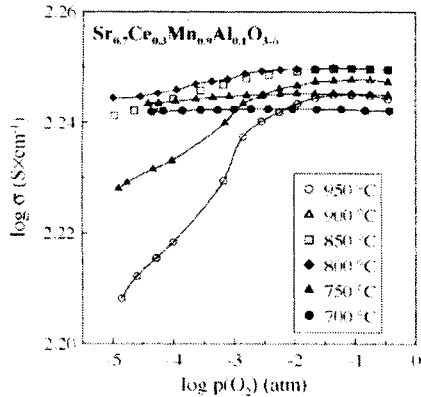


Fig. 10. Oxygen partial pressure dependencies of the total conductivity of  $\text{Sr}_{0.7}\text{Ce}_{0.3}\text{Mn}_{0.9}\text{Al}_{0.1}\text{O}_{3-\delta}$  under oxidizing conditions.

ity is expected to increase on reducing  $p(\text{O}_2)$ , the experimental data on total conductivity (Fig. 10) exhibit the opposite trend at 800–950 °C. The thermopower is negative, decreases with increasing temperature and increases on reducing  $p(\text{O}_2)$  (Fig. 11). No simple interpretation of the observed trends is possible if assuming n-type behaviour. If the conduction is dominated by the p-type charge carriers, these trends can be interpreted in terms of two processes determining hole concentration, namely thermal excitation and oxygen losses from the lattice. The first seems to play a key role at 700–750 °C, when the conductivity increases with temperature and the electrical properties are essentially  $p(\text{O}_2)$ -independent, suggesting that the oxygen nonstoichiometry is almost constant. Heating up to 900–950 °C results in extensive oxygen losses; consequently, the hole concentration becomes apparently temperature-independent at fixed  $p(\text{O}_2)$  and decrease when the oxygen pressure decreases. The corresponding variations of  $p/N$  ratio calculated by Eq. (3) are illustrated in Figs. 12 and 13. At the same time, one should mention that the variations of total conductivity and Seebeck

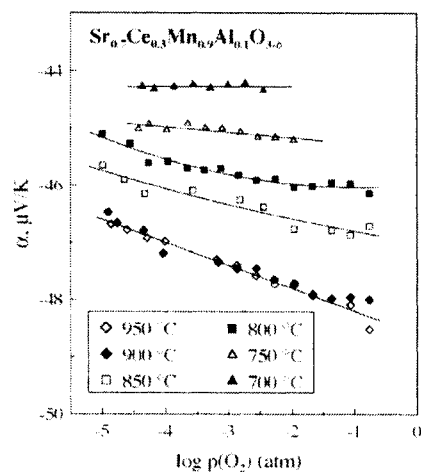


Fig. 11. Oxygen partial pressure dependencies of the Seebeck coefficient of  $\text{Sr}_{0.7}\text{Ce}_{0.3}\text{Mn}_{0.9}\text{Al}_{0.1}\text{O}_{3-\delta}$  under oxidizing conditions.

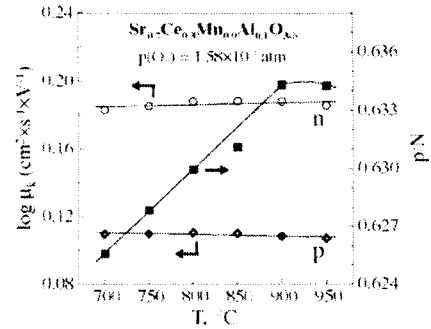


Fig. 12. Temperature dependencies of the  $p/N$  ratio and estimated mobility for the p-type and n-type electronic charge carriers in  $\text{Sr}_{0.7}\text{Ce}_{0.3}\text{Mn}_{0.9}\text{Al}_{0.1}\text{O}_{3-\delta}$  at  $p(\text{O}_2) = 1.58 \times 10^{-3}$  atm.

coefficient, shown in Figs. 10 and 11, are rather weak, which may lead to substantial uncertainties in their analysis.

Important information on the electronic conduction mechanism may also be obtained considering the temperature dependencies of charge carrier mobility ( $\mu$ ), which can be estimated using the definition<sup>32</sup>

$$\sigma = e\mu C_{RN} \tag{5}$$

where  $C_{RN}$  is the concentration of predominant charge carriers. Combining Eqs. (3) and (5) yields

$$\mu = \frac{\sigma}{eN} \left[ 1 + \exp\left(\pm \frac{\alpha e}{k}\right) \right] \tag{6}$$

with negative sign for p-type and positive for n-type behaviour. These estimations are presented in Figs. 12 and 13. Despite the type of electronic charge carriers, the mobility is almost independent of temperature, exhibiting tendency to a slight decrease on heating above 800 °C. Such a behaviour is indicative for broad-band mechanism<sup>34,35</sup> rather than for hopping conduction, for which thermally-activated mobility is typically observed.<sup>36,37</sup> Also, the values of  $\mu$ , calculated assuming the density of states to be equal to the total Mn concentration, lie within the range  $0.10\text{--}0.11 \text{ cm}^2 \text{ s}^{-1} \text{ V}^{-1}$  for p-type behaviour, and  $0.17\text{--}0.19 \text{ cm}^2 \text{ s}^{-1} \text{ V}^{-1}$  for n-type electronic transport. This level of mobility is higher than expected for a small-polaron mechanism.<sup>34–37</sup> At 900 °C,

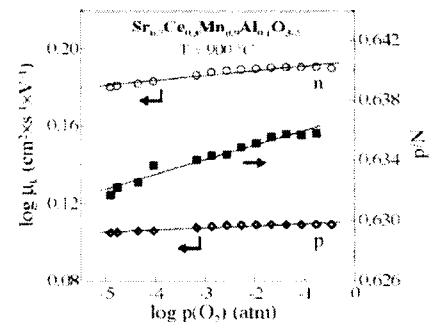


Fig. 13. Oxygen pressure dependencies of the  $p/N$  ratio and estimated mobility for the p-type and n-type electronic charge carriers in  $\text{Sr}_{0.7}\text{Ce}_{0.3}\text{Mn}_{0.9}\text{Al}_{0.1}\text{O}_{3-\delta}$  at 1173 K.

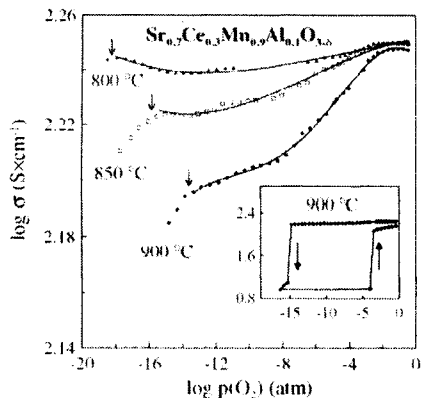


Fig. 14. Total conductivity of  $\text{Sr}_{0.7}\text{Ce}_{0.3}\text{Mn}_{0.9}\text{Al}_{0.1}\text{O}_{3-\delta}$  as function of the oxygen partial pressure. Solid lines are for visual guidance only. The arrows show approximate phase stability limits. The inset illustrates hysteresis phenomena after phase decomposition, with arrows showing the direction of  $p(\text{O}_2)$  changes.

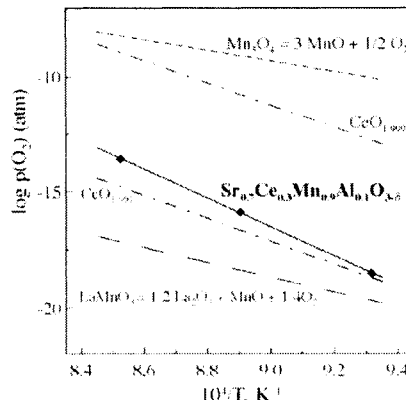


Fig. 15. Low- $p(\text{O}_2)$  stability limits of  $\text{Sr}_{0.7}\text{Ce}_{0.3}\text{Mn}_{0.9}\text{Al}_{0.1}\text{O}_{3-\delta}$ . The stability boundary for  $\text{Mn}_3\text{O}_4$ <sup>38</sup> and  $\text{LaMnO}_3$ <sup>39</sup> and iso-composition lines for  $\text{CeO}_{2-y}$ <sup>40</sup> are shown for comparison.

the  $\mu$  values tend to increase slightly with increasing oxygen chemical potential, probably due to increasing average oxidation state of Mn cations, with a corresponding decrease in their size and crystal lattice contraction. As a result, greater overlapping of manganese and oxygen electron orbitals causes a stronger covalence of the Mn–O–Mn bonds and higher degree of the electron delocalization. Similar trends are well known for other perovskite oxides.<sup>23</sup>

### 3.5. Phase stability

The perovskite phase stability limits under reducing conditions can be estimated from the abnormal drop in the total conductivity at low  $p(\text{O}_2)$  (Fig. 14). For example, at 900 °C, such a drop starts at  $p(\text{O}_2) \approx 2.6 \times 10^{-14}$  atm and is maximum at approximately  $10^{-15}$  atm. After reduction, strong hysteresis effects on redox cycling are observed, as illustrated by the inset in Fig. 14. These variations of the conductivity indicate decomposition of the perovskite-type phase, confirmed by XRD. One example of the XRD pattern of  $\text{Sr}_{0.7}\text{Ce}_{0.3}\text{Mn}_{0.9}\text{Al}_{0.1}\text{O}_{3-\delta}$  quenched after annealing in reducing atmosphere at 900 °C, is presented in Fig. 1. When temperature decreases, the decomposition occurs at lower oxygen chemical potentials, as expected.

Fig. 15 shows the approximate phase stability boundary of  $\text{Sr}_{0.7}\text{Ce}_{0.3}\text{Mn}_{0.9}\text{Al}_{0.1}\text{O}_{3-\delta}$ , evaluated from the conductivity and Seebeck coefficient data. The stability limits of  $\text{Mn}_3\text{O}_4$ ,<sup>38</sup>  $\text{LaMnO}_3$ <sup>39</sup> and two iso-concentration lines of  $\text{CeO}_{2-y}$ <sup>40</sup> are given for comparison. The decomposition of  $\text{Sr}_{0.7}\text{Ce}_{0.3}\text{Mn}_{0.9}\text{Al}_{0.1}\text{O}_{3-\delta}$  perovskite occurs at oxygen pressures close to the iso-nonstoichiometry line of  $\text{CeO}_{2-y}$  with  $y = 0.009$ , suggesting that the change in the oxidation state of cerium cations within the stability domain of  $\text{Sr}_{0.7}\text{Ce}_{0.3}\text{Mn}_{0.9}\text{Al}_{0.1}\text{O}_{3-\delta}$  should be minor. Moreover, the

estimations of  $\text{Mn}^{4+}$  fraction from the Seebeck coefficient using Eq. (4), in combination with the crystal electroneutrality and site conservation conditions, suggest that no less than 60% cerium cations are trivalent even under oxidizing conditions. Also, the ionic radii of  $\text{Ce}^{3+}$  and  $\text{Mn}^{4+}$  yield better geometrical matching for A- and B-site cations in the perovskite structure, i.e. a tolerance factor closer to unity, when compared to smaller  $\text{Ce}^{4+}$  cations in the A sublattice and larger  $\text{Mn}^{3+}$  in the B sites. The decomposition of doped strontium manganite is therefore associated with changes of the manganese oxidation state on reduction, as for  $\text{LaMnO}_{3-\delta}$ . Most likely, the formation of substantial amounts of  $\text{Mn}^{2+}$  leads to excessive stress in the lattice, followed by structural collapse.

## 4. Conclusions

Aluminum-substituted  $\text{Sr}_{0.7}\text{Ce}_{0.3}\text{MnO}_{3-\delta}$  exhibits a comparatively high oxygen ionic conduction, phase stability in a relatively wide range of conditions, sufficient level of the electronic transport, and thermal expansion compatible with that of common solid electrolytes. These properties are attractive for possible application of  $\text{Sr}_{0.7}\text{Ce}_{0.3}\text{Mn}_{1-x}\text{Al}_x\text{O}_{3-\delta}$  for SOFC cathodes. Partial substitution of Mn by Al enhances the oxygen permeability and ionic conductivity. However, as the solubility of  $\text{Al}^{3+}$  in the lattice of strontium manganite is quite low, additional doping with aliovalent cations may be desirable in order to achieve higher oxygen ionic conductivity, closer to that the solid-electrolyte materials. The dependencies of total conductivity and Seebeck coefficient on oxygen partial pressure and temperature are indicative of prevailing hole transport, with a slight conductivity increase on increasing  $p(\text{O}_2)$  and a transition from semiconducting to pseudo-metallic behaviour at temperatures above 800 °C.

392 **Acknowledgements**

393 This work was supported by the FCT, Portugal (POCTI  
394 program and project CTM/58570/2004) and by the NATO  
395 Science for Peace program (project 978002).

396 **References**

- 397 1. Singhal, S. C., Advances in solid oxide fuel cell technology. *Solid*  
398 *State Ionics*, 2000, **135**, 305.
- 399 2. Guangyao, M., Wanyu, L. and Dingkun, P., New solid state fuel  
400 cells—green power source for 21st century. *Ionics*, 1998, **4**, 451.
- 401 3. Steele, B. C. H., Material science and engineering: the enabling tech-  
402 nology for the commercialization of fuel cell systems. *J. Mater. Sci.*,  
403 2001, **36**, 1053.
- 404 4. Costamagna, P., Magistri, L. and Massardo, A. F., Design and part-  
405 lard performance of a hybrid system based on a solid oxide fuel cell  
406 reactor and a micro gas turbine. *J. Power Sources*, 2001, **96**, 352.
- 407 5. Ralph, J. M., Schoeler, A. C. and Krumpelt, M., Materials for lower  
408 temperature solid oxide fuel cells. *J. Mater. Sci.*, 2001, **36**, 1161.
- 409 6. Steele, B. C. H., Materials for IT-SOFC stacks: 35 years R&D. The  
410 inevitability of gradualness? *Solid State Ionics*, 2000, **134**, 3.
- 411 7. Perry Murray, E., Sever, M. J. and Barnett, S. A., Electrochemical  
412 performance of (La, Sr)(Co, Fe)O<sub>3-δ</sub>-(Ce, Gd)O<sub>2</sub> composite cathodes.  
413 *Solid State Ionics*, 2002, **148**, 27.
- 414 8. Qiu, L., Ichikawa, T., Hirano, A., Imanishi, N. and Takeda, Y.,  
415 Ln<sub>1-x</sub>Sr<sub>x</sub>Co<sub>1-y</sub>Fe<sub>y</sub>O<sub>3-δ</sub> (Ln=Pr, Nd, Gd; x=0.2, 0.3) for the electro-  
416 des of solid oxide fuel cells. *Solid State Ionics*, 2003, **158**, 55.
- 417 9. Kharton, V. V., Kovalevsky, A. V., Viskup, A. P., Figueiredo, F. M.,  
418 Yaremchenko, A. A., Naumovich, E. N. et al., Oxygen permeabil-  
419 ity of Ce<sub>0.8</sub>Gd<sub>0.2</sub>O<sub>2-δ</sub>-La<sub>0.7</sub>Sr<sub>0.3</sub>MnO<sub>3-δ</sub> composite membranes. *J.*  
420 *Electrochem. Soc.*, 2000, **147**, 2814.
- 421 10. Zhao, H., Huo, L. and Gao, S., Electrochemical properties of  
422 LSM-CBO composite cathode. *J. Power Sources*, 2004, **125**, 149.
- 423 11. Hashimoto, S. and Iwahara, H., Study on the structural and electrical  
424 properties of Sr<sub>1-x</sub>Ce<sub>x</sub>MnO<sub>3-α</sub> (x=0.1, 0.3) perovskite oxide. *Mater.*  
425 *Res. Bull.*, 2000, **35**, 2253.
- 426 12. Hashimoto, S. and Iwahara, H., Structural, thermal and electrical  
427 properties of Ce-doped SrMnO<sub>3</sub>. *J. Electroceram.*, 2000, **4**, 225.
- 428 13. Negas, T. and Roth, R. S., The system SrMnO<sub>3-x</sub>. *J. Solid State*  
429 *Chem.*, 1970, **1**, 409.
- 430 14. Kharton, V. V., Viskup, A. P., Marozau, I. P. and Naumovich, E.  
431 N., Oxygen permeability of perovskite-type Sr<sub>0.7</sub>Ce<sub>0.3</sub>MnO<sub>3-δ</sub>. *Mater.*  
432 *Lett.*, 2003, **57**, 3017.
- 433 15. Kharton, V. V., Figueiredo, F. M., Navarro, L., Naumovich, E. N.,  
434 Kovalevsky, A. V., Yaremchenko, A. A. et al., Ceria-based materials  
435 for solid oxide fuel cells. *J. Mater. Sci.*, 2001, **36**, 1105.
- 436 16. Kendal, K. R., Navas, C., Thomas, J. K. and zur Loye, H.-C., Recent  
437 developments in perovskite-based oxide ion conductors. *Solid State*  
438 *Ionics*, 1995, **82**, 215.
- 439 17. Stevenson, J. W., Armstrong, T. R., Carneim, R. D., Pederson, L. R.  
440 and Weber, W. J., Electrochemical properties of mixed conducting  
441 perovskites La<sub>1-x</sub>M<sub>x</sub>Co<sub>1-y</sub>Fe<sub>y</sub>O<sub>3-δ</sub> (M=Sr, Ba, Ca). *J. Electrochem.*  
442 *Soc.*, 1996, **143**, 2722.
- 443 18. Holc, J., Kuscer, D., Hrovat, M., Bernik, S. and Kolar, D., Electrical  
444 and microstructural characterisation of (La<sub>0.8</sub>Sr<sub>0.2</sub>)(Fe<sub>1-x</sub>Al<sub>x</sub>)O<sub>3</sub> and  
445 (La<sub>0.8</sub>Sr<sub>0.2</sub>)(Mn<sub>1-x</sub>Al<sub>x</sub>)O<sub>3</sub> as possible SOFC cathode materials. *Solid*  
446 *State Ionics*, 1997, **95**, 259.
- 447 19. Kharton, V. V., Yaremchenko, A. A., Patrakev, M. V., Naumovich, E.  
448 N. and Marques, F. M. B., Thermal and chemical induced expansion  
449 of La<sub>0.3</sub>Sr<sub>0.7</sub>(Fe, Ga)O<sub>3-δ</sub> ceramics. *J. Eur. Ceram. Soc.*, 2003, **23**,  
450 1417.
- 451 20. Kharton, V. V., Tikhonovich, V. N., Li Shuangbao, E. N., Naumovich,  
452 A. V., Kovalevsky, A. P., Viskup, I. A. et al., Ceramic microstructure  
453 and oxygen permeability of SrCo(Fe, M)O<sub>3-δ</sub> (M=Cu or Cr) perov-  
454 skite membranes. *J. Electrochem. Soc.*, 1998, **145**, 1363.
- 455 21. Kharton, V. V., Viskup, A. P., Kovalevsky, A. V., Figueiredo, F. M.,  
456 Jurado, J. R., Yaremchenko, A. A. et al., Surface-limited ionic trans-  
457 port in perovskites Sr<sub>0.97</sub>(Ti, Fe, Mg)O<sub>3-δ</sub>. *J. Mater. Chem.*, 2000,  
458 **10**, 1161.
- 459 22. Leonidov, I. A., Kozhevnikov, V. L., Mitberg, E. B., Patrakev, M.  
460 V., Kharton, V. V. and Marques, F. M. B., High-temperature electri-  
461 cal transport in La<sub>0.3</sub>Sr<sub>0.7</sub>Fe<sub>1-x</sub>Ga<sub>x</sub>O<sub>3-δ</sub> (x=0-0.5). *J. Mater. Chem.*,  
462 2001, **11**, 1202.
- 463 23. Patrakev, M. V., Mitberg, E. B., Lakhtin, A. A., Leonidov, I. A.,  
464 Kozhevnikov, V. L., Kharton, V. V. et al., Oxygen nonstoichiome-  
465 try, conductivity and Seebeck coefficient of La<sub>0.3</sub>Sr<sub>0.7</sub>Fe<sub>1-x</sub>Ga<sub>x</sub>O<sub>2.65-δ</sub>  
466 perovskites. *J. Solid State Chem.*, 2002, **167**, 203.
- 467 24. Shannon, R. D., Revised effective ionic radii and systematic studies of  
468 interatomic distances in halides and chalcogenides. *Acta Crystallogr.*  
469 *A*, 1976, **32**, 751.
- 470 25. Yaremchenko, A. A., Patrakev, M. V., Kharton, V. V., Marques, F. M.  
471 B., Leonidov, I. A. and Kozhevnikov, V. L., Oxygen ionic and elec-  
472 tronic conductivity of La<sub>0.3</sub>Sr<sub>0.7</sub>Fe(Al)O<sub>3-δ</sub> perovskites. *Solid State*  
473 *Sci.*, 2004, **6**, 357.
- 474 26. Tietz, F., Thermal expansion of SOFC materials. *Ionics*, 1999, **5**, 129.
- 475 27. Biebler, A. and Gauckler, L. J., In *Thermal and Isothermal Expans-*  
476 *ion in Oxygen Ion and Mixed Conductors and Their Technological*  
477 *Applications*, ed. H. L. Tuller. Kluwer Academic Publishers, 2000, p.  
478 347.
- 479 28. Bouwmeester, H. J. M. and Burggraaf, A. J., *Fundamentals of Inor-*  
480 *ganic Membrane Science and Technology*. Elsevier, 1996, p. 435.
- 481 29. Mizusaki, J., Yonemura, Y., Kamata, H., Ohyama, K., Mori, N., Takai,  
482 H. et al., Electronic conductivity, Seebeck coefficient, defect and elec-  
483 tronic structure of nonstoichiometric La<sub>1-x</sub>Sr<sub>x</sub>MnO<sub>3</sub>. *Solid State Ion-*  
484 *ics*, 2000, **132**, 167.
- 485 30. Goodenough, J. B. and Zhou, J.-S., In *Localized to Itinerant Transi-*  
486 *tion in Perovskite Oxides*, ed. J. B. Goodenough. Springer, 2001, pp.  
487 17-113.
- 488 31. *Fuel Cell Handbook (6th ed.)*. EG&G Technical Services Inc., Science  
489 Applications International Corporation, Morgantown, 2002, p. 7-1.
- 490 32. Kofstad, P., *Nonstoichiometry Diffusion and Electrical Conductivity*  
491 *in Binary Metal Oxides*. Wiley-Interscience, 1972 (Chapter 5).
- 492 33. Chaikin, P. M. and Beni, G., Thermopower in the correlated hopping  
493 regime. *Phys. Rev. B*, 1976, **13**(2), 647.
- 494 34. Appel, J., *Solid State Physics, Vol 21*. Academic Press, 1968.
- 495 35. Jonker, G. H., The application of the combined conductivity and  
496 Seebeck-effect plots for the analysis of semiconductor properties.  
497 *Philips Res. Rep.*, 1968, **23**, 131.
- 498 36. Heikes, R. R. and Johnston, W. D., Mechanism of conduction in  
499 Li-substituted transition metal oxides. *J. Chem. Phys.*, 1957, **26**, 582.
- 500 37. Nell, J., Wood, B. J., Dorris, S. E. and Mason, T. O., Jonker-type  
501 analysis of small polaron conductors. *J. Solid State Chem.*, 1989, **82**,  
502 247.
- 503 38. Charette, G. G. and Flengas, S. N., Thermodynamic properties of the  
504 oxides of Fe, Ni, Pb, Cu and Mn by EMF measurements. *J.*  
505 *Electrochem. Soc.*, 1968, **115**, 796.
- 506 39. Nakamura, T., Petzow, G. and Gauckler, L. J., Stability of the perov-  
507 skite phase LaBO<sub>3</sub> (B=V, Cr, Mn, Fe, Co Ni) in reducing atmo-  
508 sphere. I. Experimental results. *Mater. Res. Bull.*, 1979, **14**, 649.
- 509 40. Panlener, R. J. and Blumenthal, R. N., *Thermodynamic study of non-*  
510 *stoichiometric cerium dioxide*. Report no. COO-1441-18, U.S.A.E.C.,  
511 1972, pp. 1-34.
- 512 41. Kharton, V. V., Marozau, I. P., Vyshatko, N. P., Shaula, A. L., Viskup,  
513 A. P., Naumovich, E. N. et al., Oxygen ionic conduction in brown-  
514 millerite CaAl<sub>0.5</sub>Fe<sub>0.5</sub>O<sub>2.5+δ</sub>. *Mater. Res. Bull.*, 2003, **38**, 773.